Why slow axonal transport is bidirectional – can axonal transport of tau protein rely only on motor-driven anterograde transport?

Ivan A. Kuznetsov[(a), (b)] and Andrey V. Kuznetsov[(c)]

[(a)]Perelman School of Medicine, University of Pennsylvania, Philadelphia, PA 19104, USA

[(b)]Department of Bioengineering, University of Pennsylvania, Philadelphia, PA 19104, USA

[(c)]Dept. of Mechanical and Aerospace Engineering, North Carolina State University,

Raleigh, NC 27695-7910, USA; e-mail: avkuznet@ncsu.edu

Abstract

Slow axonal transport (SAT) moves multiple proteins from the soma, where they are synthesized, to the axon terminal. Due to the great lengths of axons, SAT almost exclusively relies on active transport, which is driven by molecular motors. The puzzling feature of slow axonal transport is its bidirectionality. Although the net direction of SAT is anterograde, from the soma to the terminal, experiments show that it also contains the retrograde component. One of the proteins transported by SAT is microtubule-associated protein tau. To better understand why the retrograde component in tau transport is needed, we used the perturbation technique. We analyzed the simplification of the full tau SAT model for the case when retrograde motor-driven transport and diffusion-driven transport of tau are negligible, and tau is driven only by anterograde (kinesin) motors. The solution of the simplified equations shows that the tau concentration along the axon length stays almost uniform (decreases very slightly), which is inconsistent with the tau concentration at the outlet boundary (at the axon tip). Thus kinesin-driven transport alone is not enough, and the retrograde motor-driven component in SAT is needed.

Keywords neuron; axon; mathematical modeling; kinesin; dynein

List of Abbreviations

LSR	least square regression
MT	microtubule
NF	neurofilament
SAT	slow axonal transport
SCa	slow component-a
SCb	slow component-b

1. Introduction

Due to the great length of axons, neurons have to rely on a complicated "railway" system composed of microtubules (MTs). Various cargos are transported along MTs being pooled by molecular motors. Typically, newly synthesized cargos are transported in the anterograde direction (from the soma to the axon terminal) by molecular motors that belong to the kinesin superfamily. Cargos that need to be recycled in the somatic lysosomes are transported in the retrograde direction by molecular motors that belong to the dynein superfamily. Axonal transport is classified into fast anterograde axonal transport, which is driven by kinesin motors (representative velocity 1 μm s^{-1}), fast retrograde axonal transport, which is driven by dynein motors (representative velocity is also 1 μm s^{-1}), and slow axonal transport (SAT) (Morfini et al. 2012; Brown 2016; Roy 2020; Sleigh et al. 2019; Guedes-Dias and Holzbaur 2019).

One intriguing feature of SAT is its slow velocity. Cytoskeletal elements, such as neurofilaments (NFs), which are transported in slow component-a (SCa), move with an average anterograde velocity of 0.002–0.02 μm s^{-1}. Many other cargos, such as cytosolic proteins and tau protein (hereafter tau), which are transported in slow component-b (SCb), move with an average anterograde velocity of 0.02–0.09 μm s^{-1} (Brown 2000). It is puzzling because the average velocity of anterograde and retrograde molecular motors, kinesin and dynein, is approximately 1 μm s^{-1} (Brown 2000; Goldstein 2001). This puzzle was resolved independently in Wang et al. (2000) and Roy et al. (2000) who studied SCa transport of NFs and found that these cargos alternate between fast anterograde and retrograde movements (occurring with a velocity of ~1 μm s^{-1}) and frequent pauses. A representative portion of time that NFs spend pausing is 97% (Brown 2014), which explains the small average velocity of NFs.

The second mystery of SAT is that it moves cargoes in both anterograde and retrograde directions, although it has a net anterograde bias (Brown 2014). Since moving cargoes by molecular motors requires energy, the presence of the retrograde component in SAT is puzzling since it makes cargo delivery more energetically expensive. In this paper, we used mathematical modeling to explain why slow axonal transport must be bidirectional to allow for maintenance of concentration gradients along the axon length.

Tau is mostly known for its involvement in Alzheimer's disease and other tauopathies when it becomes prone to aggregation (Huang et al. 2016; Iqbal et al. 2010; Zempell and Mandelkow 2014; Blennow et al. 2006). In axons, tau is transported by SCb (Utton et al. 2002; Utton et al. 2005; Brown 2014). In this paper, we conducted the analysis on equations in a model developed in Kuznetsov and Kuznetsov (2017, 2018, 2020) to investigate what happens when all other modes of transport except kinesin-driven transport of tau become negligible. The goal is to study whether anterograde motor-driven transport alone can simulate the experimentally obtained tau distribution reported in Black et al. (1996). Since in a

healthy neuron tau predominantly exists in the monomeric form, hereafter we denoted tau monomer as tau.

2. Materials and models

2.1. Mathematical model of tau transport in an axon

A schematic diagram of the axon is displayed in Fig. 1. Since we need equations describing tau transport for the perturbation analysis, we briefly restate here the equations developed in Kuznetsov and Kuznetsov (2017, 2018, 2020).

The model simulates tau transitions between seven different kinetic states (Fig. 2). A tau concentration in a corresponding kinetic state is given below in the parentheses. Two of the kinetic states describe active anterograde (n_a^*) and retrograde (n_r^*) transport of tau propelled by kinesin and dynein motors, respectively (Utton et al. 2005; Butler et al. 2019). Two other kinetic states are anterograde (n_{a0}^*) and retrograde (n_{r0}^*) pausing states, respectively, when motors driving the cargo temporarily disengage from MTs, but are ready to re-engage and resume their motion. There are also two kinetic states in which tau can be driven by diffusion. These are free (cytosolic) state (n_{free}^*) (Samsonov et al. 2004; Konzack et al. 2007; Weissmann et al. 2009) and a kinetic state representing a sub-population of MT-bound tau that can diffuse along the MTs (n_{dif}^*) (Hinrichs et al. 2012). There is also a sub-population of MT-bound tau that is stationary (n_{st}^*) (Hinrichs et al. 2012). Since an axon is much longer in one dimension than in the other two dimensions, all tau concentrations in the axon are represented by one-dimensional densities of tau monomers (μm^{-1}).

A Cartesian coordinate directed along the axon is denoted as x^* (Fig. 1). We used the SAT model of tau developed in Kuznetsov and Kuznetsov (2017, 2018, 2020). The model consists of seven equations obtained by stating tau conservation in the corresponding kinetic states. We assume that in a healthy axon transport processes are quasi-steady; thus $\partial \ldots / \partial t^* = 0$. The conservation of tau in anterograde and retrograde motor-driven states leads to the following equations, respectively (Fig. 2):

$$-v_a^* \frac{dn_a^*}{dx^*} - \gamma_{10}^* n_a^* + \gamma_{01}^* n_{a0}^* = 0 , \quad (1)$$

$$v_r^* \frac{dn_r^*}{dx^*} - \gamma_{10}^* n_r^* + \gamma_{01}^* n_{r0}^* = 0 , \quad (2)$$

where asterisks denote dimensional quantities. The first terms on the left-hand sides of Eqs. (1) and (2) represent the change of tau concentration in a control volume due to motor-driven transport, while the terms that are multiplied by kinetic constants ($\gamma^* s$) represent transitions of tau between motor-driven and pausing kinetic states (Fig. 2). We defined model parameters in Tables S1 and S2 in the Supplemental Materials.

Stating the conservation of tau in the pausing states, which simulate the situation when tau is temporarily disengaged from MTs, gives the following equations (Fig. 2):

$$-\left(\gamma_{01}^* + \gamma_{ar}^* + \gamma_{off,a}^*\right) n_{a0}^* + \gamma_{10}^* n_a^* + \gamma_{ra}^* n_{r0}^* + \gamma_{on,a}^* n_{free}^* = 0\,, \tag{3}$$

$$-\left(\gamma_{01}^* + \gamma_{ra}^* + \gamma_{off,r}^*\right) n_{r0}^* + \gamma_{10}^* n_r^* + \gamma_{ar}^* n_{a0}^* + \gamma_{on,r}^* n_{free}^* = 0\,. \tag{4}$$

Because tau does not move in the pausing states, tau concentrations in the pausing states can change only due to tau transitions to and from other kinetic states.

Stating the conservation of tau in the free state, which simulates the pool of tau that is freely suspended in the cytosol and is not associated with MTs, gives the following equation:

$$D_{free}^* \frac{d^2 n_{free}^*}{dx^{*2}} + \gamma_{off,a}^* n_{a0}^* + \gamma_{off,r}^* n_{r0}^* - \left(\gamma_{on,a}^* + \gamma_{on,r}^* + \gamma_{free\to st}^* + \gamma_{free\to dif}^*\right) n_{free}^* + \gamma_{st\to free}^* n_{st}^*$$

$$+\gamma_{dif\to free}^* n_{dif}^* - \frac{n_{free}^* \ln(2)}{T_{1/2}^*} = 0\,, \tag{5}$$

where the first term on the left-hand side of Eq. (5) simulates diffusion-driven transport of tau in the cytosol, and the last term on the left-hand side of Eq. (5) simulates tau degradation in proteasomes (Poppek et al. 2006; Kierszenbaum 2000). The tau degradation term is only included for the free (cytosolic) tau because tau must be detached from MTs to enter a proteasome's proteolytic chamber. All other terms in Eq. (5) simulate tau transitions to/from the free cytosolic state.

It is important to mention that the model considers two possible mechanisms of tau protein transition between a retrograde pausing state (bound to dynein) and an anterograde pausing state (bound to kinesin), see Fig. 2. (i) Tau protein can first unbind from a kinesin and then bind to a dynein. In this case, the transition is through the free state. (ii) Tau protein bound to kinesin can be directly "stolen" by a dynein (and bind to this dynein), see Eqs. (3) and (4).

Tau that is attached to MTs can be divided into stationary tau and tau that can diffuse along the MTs (Hinrichs et al. 2012). Stating the conservation of the diffusing fraction of MT-bound tau gives the following equation:

$$D_{mt}^{*}\frac{d^{2}n_{dif}^{*}}{dx^{*2}}-\left(\gamma_{dif\to free}^{*}+\gamma_{dif\to st}^{*}\right)n_{dif}^{*}+\gamma_{free\to dif}^{*}n_{free}^{*}+\gamma_{st\to dif}^{*}n_{st}^{*}=0\,. \tag{6}$$

The first term on the left-hand side of Eq. (6) simulates transport of tau by its diffusion along MTs. All other terms simulate transitions to/from the kinetic state representing tau diffusing along MTs (Fig. 2).

Part of tau attached to MTs is stationary (Hinrichs et al. 2012), and stating tau conservation in the stationary kinetic state leads to the following equation:

$$-\left(\gamma_{st\to free}^{*}+\gamma_{st\to dif}^{*}\right)n_{st}^{*}+\gamma_{free\to st}^{*}n_{free}^{*}+\gamma_{dif\to st}^{*}n_{dif}^{*}=0\,. \tag{7}$$

Since tau in the stationary state does not move, its concentration can only change due to tau transitions to/from the stationary state (Fig. 2).

The total tau concentration is calculated by finding the sum of tau concentrations in all seven kinetic states (Fig. 2):

$$n_{tot}^{*}=n_{a}^{*}+n_{r}^{*}+n_{a0}^{*}+n_{r0}^{*}+n_{free}^{*}+n_{st}^{*}+n_{dif}^{*}\,. \tag{8}$$

Tau is associated with MTs in six out of seven kinetic states (except for n_{free}^{*}). The percentage of MT-bound tau is found by calculating the ratio of the sum of tau concentrations in six MT-associated states to n_{tot}^{*}:

$$\%\text{bound}=\frac{n_{a}^{*}+n_{r}^{*}+n_{a0}^{*}+n_{r0}^{*}+n_{st}^{*}+n_{dif}^{*}}{n_{tot}^{*}}\left(100\%\right). \tag{9}$$

Tau can be driven by four mechanisms: anterograde transport by kinesin motors, retrograde transport by dynein motors, diffusion of free tau in the cytosol, and diffusion of MT-bound tau along MTs. The total flux of tau can be found as:

$$j_{tot}^{*}=v_{a}^{*}n_{a}^{*}-v_{r}^{*}n_{r}^{*}-D_{free}^{*}\frac{dn_{free}^{*}}{dx^{*}}-D_{mt}^{*}\frac{dn_{dif}^{*}}{dx^{*}}\,. \tag{10}$$

The average tau velocity was found as suggested in Kuznetsov and Kuznetsov (2015):

$$v_{av}^{*}\left(x^{*}\right)=\frac{j_{tot}^{*}}{n_{tot}^{*}}. \tag{11}$$

Eqs. (1)-(7) require six boundary conditions. We imposed three boundary conditions at the axon hillock:

$$\text{At } x^{*}=0:\ j_{tot}^{*}\Big|_{x=0}=j_{tot,x=0}^{*},\ n_{free}^{*}\Big|_{x=0}=n_{free,x=0}^{*},\ n_{tot}^{*}\Big|_{x=0}=n_{tot,x=0}^{*}, \tag{12a,b,c}$$

which postulate the tau flux into the axon, the concentration of free tau at the axon hillock, and the total concentration of tau at the axon hillock, respectively. $j_{tot,x=0}$ and $n_{free,x=0}$ are determined by finding values that give the best fit between model predictions and published experimental results (Table S2).

The following three boundary conditions were imposed at the axon terminal:

$$\text{At } x^{*}=L^{*}:\ \frac{dn_{free}^{*}}{dx^{*}}\Bigg|_{x=L}=0,\ n_{tot}^{*}\Big|_{x=L}=n_{tot,55}^{*},\ j_{tot}^{*}=j_{tot,x=L}^{*}, \tag{13a,b,c}$$

which postulate zero concentration gradient of free tau at the axon tip, the total tau concentration at the axon tip, and the flux of tau into the axon terminal, respectively. The flux of tau into the axon terminal, $j_{tot,x=L}^{*}$, in Eq. (13c) was calculated according to Eq. (S1), see section S2 in the Supplemental Materials.

Some of the values of the model parameters can be found in the literature; these are summarized in Table S1. Other parameters whose values are not found in the literature (for example kinetic constants characterizing the rates of tau transitions between different kinetic states, $\gamma^{*}s$) are summarized in Table S2. These parameters in Table S2 were determined by finding values that give the best fit with published experimental data. Our problem involves different types of published data, for example, the tau concentration and velocity. Therefore, we used multi-objective optimization (Kool et al. 1987; Zadeh 2008; Zadeh and Shah 2010; Zadeh 2011; Zadeh and Montas 2014) to determine best-fit values of these parameters in Table S2. The following objective (penalty) function, which characterizes the deviation of model predictions from published data, was utilized:

$$err=\sum_{j=1}^{N}\left(n_{tot,j}-n_{tot,exper,j}\right)^{2}+\omega_{1}\sum_{j=1}^{N}\left(v_{av,j}^{*}-0.00345\frac{\mu\text{m}}{\text{s}}\right)^{2}+\omega_{2}\left(\%\text{bound}\Big|_{x=L/2}-100\right)^{2}+\omega_{3}, \tag{14}$$

where the dimensionless total tau concentration as well as other dimensionless parameters are defined in Table S3. Eqs. (1)-(7) with boundary conditions (12), (13) were solved for various values of parameters given in Table S2. This was done until the values of parameters that give the global minimum to the

objective function defined in Eq. (14) were found. More details about the minimization algorithm are given in section S3.

The first term on the right-hand side of Eq. (14) characterizes the deviation between the predicted and experimentally measured tau concentrations along the axon length. The experimentally measured concentration was obtained by scanning the tau concentration data reported in Fig. 7D of Black et al. (1996) in 55 (N=55) experimental points.

The second term on the right-hand side of Eq. (14) characterizes the deviation between the predicted velocity of tau transport (see Eq. (11)) and the average of the reported range of tau velocity (0.2-0.4 mm/day, Mercken et al. (1995), Scholz and Mandelkow (2014)).

The third term on the right-hand side of Eq. (14) is utilized to simulate that most of tau must be attached to MTs. (According to Janning et al. (2014), approximately 99% of tau is bound to MTs.) We set ω_1 =10,000 $s^2/\mu m^2$ and ω_2 =1. This was done based on extensive numerical trials to avoid overfitting the tau concentration, average velocity, or the percentage of MT-bound tau. Note that due to dimensions of ω_1 the second term on the right-hand side of Eq. (14) is dimensionless.

The fourth term on the right-hand side of Eq. (14) prevents tau concentrations in any of the kinetics states displayed in Fig. 2 from becoming negative, which would be unphysical. The non-negative values were achieved by setting ω_3 to a large positive value, 10^8, if any of $n_{a,j}$, $n_{r,j}$, $n_{a0,j}$, $n_{r0,j}$, $n_{free,j}$, $n_{dif,j}$, or $n_{st,j}$ at any location in the axon (j=1,…,55) becomes negative. Otherwise, ω_3 was set to zero. This allowed the reformulation of a constrained optimization problem with a non-negative constraint into an unconstrained optimization problem with a penalty function (Yang and Huang 2004).

Numerical solution procedure of Eqs. (1)-(7) is outlined in section S3. The method of finding the best-fit values of parameters given in Table S2 by minimizing the penalty function given by Eq. (14) is also described in section S3.

2.2. A perturbation solution of the tau transport model for the case of small dynein velocity and small tau diffusivity

We are interested in investigating whether the model can simulate cargo transport against the cargo's concentration gradient by kinesin-driven transport alone. This requires setting the dynein velocity and the tau diffusivity, both in the cytosolic state and in the state that represents tau that diffuses along MTs, to

small values. For this purpose, the following small parameters were introduced. The dimensionless retrograde velocity was defined as:

$$v_r = \frac{v_r^*}{v_a^*}. \tag{15}$$

The dimensionless cargo diffusivity in the cytosolic state is defined as:

$$D_{free} = \frac{D_{free}^*}{v_a^* L^*}. \tag{16}$$

The right-hand side of Eq. (16) represents the reciprocal to the Peclet number. Eq. (16) can be re-written as:

$$D_{free} = \frac{L^* / v_a^*}{L^{*2} / D_{free}^*}. \tag{17}$$

Thus, D_{free} can be viewed as the ratio of the convection time to diffusion time for free tau.

Similarly, the dimensionless cargo diffusivity of MT-bound tau that diffuses alone MTs is defined as:

$$D_{mt} = \frac{D_{mt}^*}{v_a^* L^*}. \tag{18}$$

Since

$$D_{mt} = \frac{L^* / v_a^*}{L^{*2} / D_{mt}^*}, \tag{19}$$

D_{mt} can be interpreted as the ratio of the convection time to diffusion time of MT-diffusing tau.

If the dynein velocity is small, v_r can be treated as a small parameter. For seven dependent variables of the model, n_a^*, n_r^*, n_{a0}^*, n_{r0}^*, n_{free}^*, n_{dif}^*, and n_{st}^*, we used the following perturbation expansions (for example):

$$n_a^* = n_a^{*(0)} + v_r n_a^{*(1)} + \ldots \tag{20}$$

We then substituted the perturbation expansions (such as Eq. (20)) for all seven dependent variables into Eqs. (1)-(7). We separated the terms that do and do not contain the small parameter v_r in the obtained equations and equated the terms that do not contain v_r to zero. As a result, Eqs. (S2)-(S8) were obtained.

If the diffusivity of cytosolic tau is small, D_{free} can be treated as a small parameter. For seven dependent variables of the model, $n_a^{*(0)}$, $n_r^{*(0)}$, $n_{a0}^{*(0)}$, $n_{r0}^{*(0)}$, $n_{free}^{*(0)}$, $n_{dif}^{*(0)}$, and $n_{st}^{*(0)}$, we used the following perturbation expansions (for example):

$$n_a^{*(0)} = n_a^{*(0,0)} + D_{free} n_a^{*(0,1)} + \ldots \tag{21}$$

We then substituted the perturbation expansions (such as Eq. (21)) for all seven dependent variables into Eqs. (S2)-(S8). We separated the terms that do and do not contain the small parameter D_{free} in the obtained equations, and equated the terms that do not contain D_{free} to zero. As a result, Eqs. (S9)-(S15) were obtained.

If the diffusivity of MT-bound tau is small, D_{mt} can be treated as a small parameter. For seven dependent variables of the model, $n_a^{*(0,0)}$, $n_r^{*(0,0)}$, $n_{a0}^{*(0,0)}$, $n_{r0}^{*(0,0)}$, $n_{free}^{*(0,0)}$, $n_{dif}^{*(0,0)}$, and $n_{st}^{*(0,0)}$, we used the following perturbation expansions (for example):

$$n_a^{*(0,0)} = n_a^{*(0,0,0)} + D_{mt} n_a^{*(0,0,1)} + \ldots \tag{22}$$

We then substituted the perturbation expansions (such as Eq. (22)) for all seven dependent variables into Eqs. (S9)-(S15). We separated the terms that do and do not contain the small parameter D_{mt} in the obtained equations and equated the terms that do not contain D_{mt} to zero. As a result, Eqs. (S16)-(S22) were obtained.

To simplify the notations, we replaced the superscript (0,0,0) with [0]. By solving Eq. (S17) for $n_{r0}^{*[0]}$, the following equation was obtained:

$$n_{r0}^{*[0]} = \frac{\gamma_{10}^*}{\gamma_{01}^*} n_r^{*[0]}. \tag{23}$$

We used Eq. (23) to eliminate $n_{r0}^{*[0]}$ from Eqs. (S16), (S18)-(S22), and obtained Eqs. (S23)-(S28).

By eliminating $n_r^{*[0]}$, $n_{a0}^{*[0]}$, $n_{free}^{*[0]}$, $n_{dif}^{*[0]}$, and $n_{st}^{*[0]}$ from Eqs. (S23)-(S28), we obtained the following equation for $n_a^{*[0]}$:

$$\gamma_{10}^* n_a^{*[0]} \ln(2)\left[\gamma_{ar}^* \gamma_{off,r}^* + \gamma_{off,a}^*\left(\gamma_{off,r}^* + \gamma_{ra}^*\right)\right] + \frac{dn_a^{*[0]}}{dx^*}\left[\ln(2)\left(\gamma_{off,r}^*\left(\gamma_{01}^* + \gamma_{ar}^* + \gamma_{off,a}^*\right) + \gamma_{ra}^*\left(\gamma_{01}^* + \gamma_{off,a}^*\right)\right)\right.$$

$$+\gamma_{01}^{*}T_{1/2}^{*}\left(\gamma_{off,r}^{*}\gamma_{on,a}^{*}+\gamma_{ra}^{*}\left(\gamma_{on,a}^{*}+\gamma_{on,r}^{*}\right)\right)\Big]=0\,. \tag{24}$$

To compare the numerical solution of Eqs. (1)-(7) and the analytical solution of the perturbation equations (S15)-(S21) we have to be selective about the boundary condition. While Eqs. (1)-(7) require six boundary conditions, which are postulated by Eqs. (12) and (13), the perturbation equations (S15)-(S21) allow for only one boundary condition. To compare the two solutions, we assumed the same rate of tau synthesis in the soma. This results in the same tau flux from the soma into the axon, $j_{tot,x=0}^{*}$. We thus solved Eq. (24) subject to the following boundary condition, which is identical to Eq. (12a):

$$\text{At } x^{*}=0:\ j_{tot,x=0}^{*}=v_{a}^{*}n_{a,0}^{*(0)}\left(0\right). \tag{25}$$

Eq. (25) is valid because in the kinesin-only transport model, the flux of tau is calculated as:

$$j_{tot}^{*}\left(x^{*}\right)=v_{a}^{*}n_{a}^{*}. \tag{26}$$

The solution of Eq. (24) subject to boundary condition (25) is

$$n_{a}^{*[0]}=\frac{j_{tot,x=0}^{*}}{v_{a}^{*}}\exp\left[-\frac{a}{b}x^{*}\right], \tag{27}$$

where

$$a=\ln(2)\gamma_{10}^{*}\left(\gamma_{ar}^{*}\gamma_{off,r}^{*}+\gamma_{off,a}^{*}\left(\gamma_{off,r}^{*}+\gamma_{ra}^{*}\right)\right), \tag{28}$$

and

$$b=\gamma_{01}^{*}T_{1/2}^{*}v_{a}^{*}\left(\gamma_{off,r}^{*}\gamma_{on,a}^{*}+\gamma_{ra}^{*}\left(\gamma_{on,a}^{*}+\gamma_{on,r}^{*}\right)\right)+v_{a}^{*}\ln(2)\left[\gamma_{off,r}^{*}\left(\gamma_{01}^{*}+\gamma_{ar}^{*}+\gamma_{off,a}^{*}\right)+\gamma_{ra}^{*}\left(\gamma_{01}^{*}+\gamma_{off,a}^{*}\right)\right]. \tag{29}$$

Solving Eq. (S23) for $n_{a0}^{*[0]}$, the following is obtained:

$$n_{a0}^{*[0]}=\frac{1}{\gamma_{01}^{*}}\left(\gamma_{10}^{*}n_{a}^{*[0]}+\frac{dn_{a}^{*[0]}}{dx^{*}}v_{a}^{*}\right). \tag{30}$$

By eliminating $n_{free}^{*[0]}$, $n_{dif}^{*[0]}$, and $n_{st}^{*[0]}$ from Eqs. (S24), (S25), (S27), and (S28), the following equation for $n_{r}^{*[0]}$ is obtained:

$$n_r^{*[0]} = \frac{\gamma_{01}^* n_{a0}^{*[0]} \left[\gamma_{on,r}^* \left(\gamma_{01}^* + \gamma_{ar}^* + \gamma_{off,a}^* \right) + \gamma_{ar}^* \gamma_{on,a}^* \right] - \gamma_{01}^* \gamma_{10}^* \gamma_{on,r}^* n_a^{*[0]}}{\gamma_{10}^* \gamma_{off,r}^* \gamma_{on,a}^* + \gamma_{10}^* \gamma_{ra}^* \left(\gamma_{on,a}^* + \gamma_{on,r}^* \right)} . \tag{31}$$

It should be noted that although the perturbation solution is obtained for $v_r \to 0$, the tau concentration $n_r^{*[0]}$ is still defined, tau just does not move into this kinetic state. The same applies to tau concentrations in the diffusion-driven states, $n_{free}^{*[0]}$ and $n_{dif}^{*[0]}$.

By eliminating $n_r^{*[0]}$, $n_{dif}^{*[0]}$, and $n_{st}^{*[0]}$ from Eqs. (S24), (S25), (S27), and (S28), the following equation for $n_{free}^{*[0]}$ is obtained:

$$n_{free}^{*[0]} = \frac{-\gamma_{10}^* n_a^{*[0]} \left(\gamma_{off,r}^* + \gamma_{ra}^* \right) + \gamma_{off,r}^* n_{a0}^{*[0]} \left(\gamma_{01}^* + \gamma_{ar}^* + \gamma_{off,a}^* \right) + \gamma_{ra}^* n_{a0}^{*[0]} \left(\gamma_{01}^* + \gamma_{off,a}^* \right)}{\gamma_{off,r}^* \gamma_{on,a}^* + \gamma_{ra}^* \left(\gamma_{on,a}^* + \gamma_{on,r}^* \right)} . \tag{32}$$

By eliminating $n_r^{*[0]}$, $n_{free}^{*[0]}$, and $n_{st}^{*[0]}$ from Eqs. (S24), (S25), (S27), and (S28), the following equation for $n_{dif}^{*[0]}$ is obtained:

$$\begin{aligned} n_{dif}^{*[0]} &= \left[\gamma_{free \to dif}^* \left(\gamma_{st \to dif}^* + \gamma_{st \to free}^* \right) + \gamma_{free \to st}^* \gamma_{st \to dif}^* \right] \\ &\times \frac{\left[-\gamma_{10}^* n_a^{*[0]} \left(\gamma_{off,r}^* + \gamma_{ra}^* \right) + \gamma_{off,r}^* n_{a0}^{*[0]} \left(\gamma_{01}^* + \gamma_{ar}^* + \gamma_{off,a}^* \right) + \gamma_{ra}^* n_{a0}^{*[0]} \left(\gamma_{01}^* + \gamma_{off,a}^* \right) \right]}{\xi} \end{aligned} \tag{33}$$

where

$$\xi = \left[\gamma_{dif \to free}^* \left(\gamma_{st \to dif}^* + \gamma_{st \to free}^* \right) + \gamma_{dif \to st}^* \gamma_{st \to free}^* \right] \left[\left(\gamma_{off,r}^* \gamma_{on,a}^* + \gamma_{ra}^* \left(\gamma_{on,a}^* + \gamma_{on,r}^* \right) \right) \right]. \tag{34}$$

By eliminating $n_r^{*[0]}$, $n_{free}^{*[0]}$, and $n_{dif}^{*[0]}$ from Eqs. (S24), (S25), (S27), and (S28), the following equation for $n_{st}^{*[0]}$ is obtained:

$$\begin{aligned} n_{st}^{*[0]} &= \left[\gamma_{dif \to free}^* \gamma_{free \to st}^* + \gamma_{dif \to st}^* \left(\gamma_{free \to dif}^* + \gamma_{free \to st}^* \right) \right] \\ &\times \frac{\left[-\gamma_{10}^* n_a^{*[0]} \left(\gamma_{off,r}^* + \gamma_{ra}^* \right) + \gamma_{off,r}^* n_{a0}^{*[0]} \left(\gamma_{01}^* + \gamma_{ar}^* + \gamma_{off,a}^* \right) + \gamma_{ra}^* n_{a0}^{*[0]} \left(\gamma_{01}^* + \gamma_{off,a}^* \right) \right]}{\xi} \end{aligned} \tag{35}$$

3. Results

In all numerically obtained figures in this paper (all figures except the definition sketches given in Figs. 1 and 2), we used the same values for parameters given in Table S1 to compute the curves that represent the full SAT model and the model that accounts for anterograde (kinesin-driven) transport only. This is done to enable a comparison between predictions of the two models. The values of the parameters in Table S2 are computed as values that minimize the penalty function given by Eq. (14). Note a good agreement between the model predictions and experimental results, which suggests that the optimization procedure described in section S3 worked correctly. The same values of these parameters are then used for computing the curves representing the anterograde-only transport model. This is done to ensure that the physical consequences of removing the dynein velocity and tau diffusivity from the model are not masked by the curve-fitting procedure. The curve-fitting procedure attempts to adjust the parameter values to minimize the discrepancy between the results of the model and the experimental results.

All tau concentrations were non-dimensionalized by dividing them by the total tau concentration at the axon hillock (at $x^* = 0$), as shown in Table S3. The full SAT model can simulate experimentally predicted variation of the total tau concentration perfectly well. However, a model that accounts only for kinesin-driven transport predicts a uniform distribution of tau along the axon length (Fig. 3a), which suggests that an additional tau transport mechanism is needed to simulate a variation of tau concentration along the axon length.

Both the full SAT model and kinesin-only driven model assume the same flux of tau entering the axon from the soma (see Eqs. (12a) and (25)). This explains why both curves in Fig. 3b cross at $x^* = 0$. A little faster decay of the curve depicting the tau flux predicted by the full SAT model (Fig. 3b) occurs because tau can be degraded in proteasomes only in the free (cytosolic) state, and the full SAT model predicts a larger concentration of tau in the free state than that predicted by the anterograde-only model (Fig. 4a).

According to the full SAT model, the following trends are predicted. The concentrations of anterograde and retrograde motor-driven tau stay constant over most of the axon, then sharply increase close to the axon terminal (Fig. S1). Distributions of anterograde and retrograde pausing tau behave similarly (Fig. S2). Concentrations of diffusing and stationary MT-bound tau first decrease, then linearly increase, and then decrease again. This suggests that tau diffusion works against anterograde kinesin-driven transport of tau over most of the axon (Fig. S3). If the model accounts only for anterograde kinesin-driven transport of tau, all the above tau concentrations are predicted to be uniform along the axon length (Figs. S1-S3).

The average velocity of tau transport is calculated as the ratio of the total flux of tau to the total tau concentration (Eq. (11)). The flux of tau decays very slowly due to a small rate of tau degradation in proteasomes (Fig. 3b). Therefore, the average velocity of tau (Fig. 4b) is inversely proportional to the

total tau concentration displayed in Fig. 3a. This explains the shape of the tau average velocity for the full SAT model. For the anterograde-only transport model, the average tau velocity is given by a horizontal line (Fig. 4b).

The percentage of MT-bound tau, defined by Eq. (9), is close to 100% over the whole length of the axon (Fig. 5a). This is because the best-fit values of model parameters given in Table S2 are computed such that this criterion would be satisfied (see the third term of the penalty function defined by Eq. (14)).

In Fig. 5b we plotted the distributions of the total tau concentration and seven of its components predicted by the model that accounts only for kinesin-driven transport of tau. For the parameter values given in Tables S1 and S2, $\frac{a}{b}$ in Eq. (27) equals to 1.34×10^{-9} μm^{-1}, which means that n_a is almost uniform, as shown in Fig. 5b. A slight decay of n_a is caused by a non-infinite half-life of tau. If the half-life of tau is increased to 2.16×10^{10} s (which is practically infinite), $\frac{a}{b}$ in Eq. (27) decreases to 1.37×10^{-14} μm^{-1}. The same applies to tau concentrations in all other kinetic states. Since the total tau concentration is the sum of tau concentrations in all kinetic states, the total tau concentration is also uniformly distributed along the axon length (Fig. 5b). Hence, to simulate a variation of tau concentration along the axon length, another tau transport mechanism, in addition to kinesin-driven transport, is needed.

4. Discussion, limitations of the approach, and future directions

Experimental studies conducted by Wang et al. (2000) and Roy et al. (2000) have independently demonstrated that slow axonal transport includes both anterograde and retrograde transport, with long pauses in between motor-driven motions of cargo. However, why slow axonal transport has two components (anterograde and retrograde) remains a mystery. Our findings suggest that cargo distribution experimentally observed in slow axonal transport cannot be reproduced without retrograde transport or diffusion. Since the diffusivity of most of the slow axonal transport cargos during their axonal transport is small, this explains why retrograde transport is necessary for slow axonal transport.

To validate our hypothesis, we used the following approach. We utilized the full model of slow axonal transport (given by Eqs. (1)-(7)), numerically solved it, and optimized a penalty function to determine unknown parameters. We investigated which equations the full slow axonal transport model reduces to if retrograde motor-driven transport and tau diffusion become negligibly small. In this scenario, the only remaining mechanism for tau transport in the axon is kinesin-driven anterograde transport. Then we

analytically solved Eqs. (S16)-(S22) of the reduced model with the inferred parameters. Finally, we compared the solutions of both models to published experimental measurements and determined that the reduced model without retrograde transport and diffusion was unable to adequately fit the experimental results. Indeed, the reduced model resulted in uniform tau concentrations in all kinetic states along the length of the axon (as shown in Fig. 5b). It became evident that a model that only considers anterograde motor-driven transport cannot simulate the prescribed tau variation along the axon length.

The reason is that Eqs. (S16)-(S22) contain only one ordinary differential equation, Eq. (S16). The rest of the equations are algebraic equations. The system is thus of the first order and allows only one boundary condition, which must be imposed at the axon hillock (at $x^* = 0$). As we suggested in Kuznetsov and Kuznetsov (2022a, 2022b) (for α-synuclein) and in Kuznetsov and Kuznetsov (2022c) (for MAP1B), to be able to simulate a given cargo distribution in the axon, the model must allow for the imposition of the second boundary condition, which would allow to postulate a prescribed cargo concentration at the terminal (at $x^* = L^*$). Thus, a model that accounts for anterograde motor-driven transport alone cannot simulate a prescribed cargo variation in the axon. To simulate a prescribed variation of cargo concentration, the model must account for the second transport mechanism. For long-range transport, diffusion is not a good candidate for the second mechanism because it would take an extremely long time to transport a protein particle by a distance corresponding to the length of the axon. The only remaining choice for the second mechanism is then retrograde dynein-driven transport. This conclusion has an important implication. It suggests why slow axonal transport is bidirectional, and why it contains both anterograde and retrograde motor-driven components. This is needed to support a cargo concentration that increases along the axon length, which requires cargo transport against its diffusion-driven flux.

Current research is limited because we used a continuum model for simulating cargo (tau) transport in the axon. Future research should involve simulating each cargo as an individual particle (Lai et al. 2018). This would enable further testing of our hypothesis that anterograde-only motor-driven transport is insufficient for supporting cargo transport against its concentration gradient (when the cargo concentration at the tip of the axon is larger than at its hillock), and an additional transport mechanism, such as retrograde motor-driven cargo transport, is needed to support cargo transport in this situation.

Acknowledgment

IAK acknowledges the fellowship support of the Paul and Daisy Soros Fellowship for New Americans and the NIH/National Institute of Mental Health (NIMH) Ruth L. Kirchstein NRSA (F30 MH122076-01).

AVK acknowledges the support of the National Science Foundation (award CBET-2042834) and the Alexander von Humboldt Foundation through the Humboldt Research Award.

References

Beck JV, Arnold KJ. 1977. Parameter estimation in science and engineering. New York: Wiley.

Black MM, Slaughter T, Moshiach S, Obrocka M, Fischer I. 1996. Tau is enriched on dynamic microtubules in the distal region of growing axons. Journal of Neuroscience. 16:3601-3619.

Blennow K, de Leon MJ, Zetterberg H. 2006. Alzheimer's disease. Lancet. 368:387-403.

Brown A. 2000. Slow axonal transport: Stop and go traffic in the axon. Nature Reviews Molecular Cell Biology. 1:153-156.

Brown, A. (2014). Slow axonal transport. *Reference module in biomedical sciences*. Elsevier. doi:https://doi.org/10.1016/B978-0-12-801238-3.04765-6

Brown, A. (2016). Axonal transport. In D. Pfaff, & N. Volkow (Eds.), *Neuroscience in the 21st century* (pp. 333-379) Springer. doi:10.1007/978-1-4939-3474-4_14

Butler VJ, Salazar DA, Soriano-Castell D, Alves-Ferreira M, Dennissen FJA, Vohra M, Oses-Prieto JA, Li KH, Wang AL, Jing B, Li B, Groisman A, Gutierrez E, Mooney S, Burlingame AL, Ashrafi K, Mandelkow E, Encalada SE, Kao AW. 2019. Tau/MAPT disease-associated variant A152T alters tau function and toxicity via impaired retrograde axonal transport. Human Molecular Genetics. 28:1498-1514.

Dantzig GB, Thapa MN. 2003. Linear programming 2: Theory and extensions. New York: Springer.

Goldstein LSB. 2001. Kinesin molecular motors: Transport pathways, receptors, and human disease. Proceedings of the National Academy of Sciences of the United States of America. 98:6999-7003.

Guedes-Dias P, Holzbaur ELF. 2019. Axonal transport: Driving synaptic function. Science. 366:eaaw9997.

Hinrichs MH, Jalal A, Brenner B, Mandelkow E, Kumar S, Scholz T. 2012. Tau protein diffuses along the microtubule lattice. The Journal of Biological Chemistry. 287:38559-68.

Huang Y, Wu Z, Zhou B. 2016. Behind the curtain of tauopathy: A show of multiple players orchestrating tau toxicity. Cellular and Molecular Life Sciences. 73:1-21.

Igaev M, Janning D, Suendermann F, Niewidok B, Brandt R, Junge W. 2014. A refined reaction-diffusion model of tau-microtubule dynamics and its application in FDAP analysis. Biophysical Journal. 107:2567-2578.

Iqbal K, Liu F, Gong C-, Grundke-Iqbal I. 2010. Tau in Alzheimer disease and related tauopathies. Current Alzheimer Research. 7:656-664.

Janning D, Igaev M, Suendermann F, Bruehmann J, Beutel O, Heinisch JJ, Bakota L, Piehler J, Junge W, Brandt R. 2014. Single-molecule tracking of tau reveals fast kiss-and-hop interaction with microtubules in living neurons. Molecular Biology of the Cell. 25:3541-3551.

Kierszenbaum A. 2000. The 26S proteasome: Ubiquitin-mediated proteolysis in the tunnel. Molecular Reproduction and Development. 57:109-110.

Konzack S, Thies E, Marx A, Mandelkow EM, Mandelkow E. 2007. Swimming against the tide: Mobility of the microtubule-associated protein tau in neurons. Journal of Neuroscience. 27:9916-9927.

Kool JB, Parker JC, van Genuchten MT. 1987. Parameter estimation for unsaturated flow and transport models - A review. Journal of Hydrology. 91:255-293.

Kuznetsov IA, Kuznetsov AV. 2022a. Bidirectional, unlike unidirectional transport, allows transporting axonal cargos against their concentration gradient. Journal of Theoretical Biology. 546:111161.

Kuznetsov IA, Kuznetsov AV. 2015. A comparison between the diffusion-reaction and slow axonal transport models for predicting tau distribution along an axon. Mathematical Medicine and Biology. 32:263-283.

Kuznetsov IA, Kuznetsov AV. 2017. Simulating tubulin-associated unit transport in an axon: Using bootstrapping for estimating confidence intervals of best fit parameter values obtained from indirect experimental data. Proceedings of the Royal Society A. 473:20170045.

Kuznetsov IA, Kuznetsov AV. 2018. Simulating the effect of formation of amyloid plaques on aggregation of tau protein. Proceedings of the Royal Society A-Mathematical Physical and Engineering Sciences. 474:20180511.

Kuznetsov IA, Kuznetsov AV. 2022b. Computational investigation of the effect of reduced dynein velocity and reduced cargo diffusivity on slow axonal transport. Proceedings of the Royal Society A. in press, bioRxiv, https://biorxiv.org/cgi/content/short/2022.10.14.512302.

Kuznetsov IA, Kuznetsov AV. 2022c. Dynein dysfunction prevents maintenance of high concentrations of slow axonal transport cargos at the axon terminal. ASME Journal of Biomechanical Engineering. in press, bioRxiv, https://biorxiv.org/cgi/content/short/2022.06.19.496644.

Kuznetsov IA, Kuznetsov A, V. 2020. Modeling tau transport in the axon initial segment. Mathematical Biosciences. 329:108468.

Lai X, Brown A, Xue C. 2018. A stochastic model that explains axonal organelle pileups induced by a reduction of molecular motors. Journal of the Royal Society Interface. 15:20180430.

Li Y, Jung P, Brown A. 2012. Axonal transport of neurofilaments: A single population of intermittently moving polymers. Journal of Neuroscience. 32:746-758.

Mercken M, Fischer I, Kosik K, Nixon R. 1995. Three distinct axonal transport rates for tau, tubulin, and other microtubule-associated proteins: Evidence for dynamic interactions of tau with microtubules in vivo. Journal of Neuroscience. 15:8259-8267.

Morfini, G. A., Burns, M. R., Stenoien, D. L., and Brady, S. T. (2012). Axonal transport. In S. T. Brady, G. J. Siegel, R. W. Albers & D. L. Price (Eds.), *Basic neurochemistry: Principles of molecular, cellular, and medical neurobiology* (8th ed., pp. 146-164). Amsterdam: Elsevier.

Poppek D, Keck S, Ermak G, Jung T, Stolzing A, Ullrich O, Davies KJA, Grune T. 2006. Phosphorylation inhibits turnover of the tau protein by the proteasome: Influence of RCAN1 and oxidative stress. Biochemical Journal. 400:511-520.

Roy S, Coffee P, Smith G, Liem RKH, Brady ST, Black MM. 2000. Neurofilaments are transported rapidly but intermittently in axons: Implications for slow axonal transport. Journal of Neuroscience. 20:6849-6861.

Roy S. 2020. Finding order in slow axonal transport. Current Opinion in Neurobiology. 63:87-94.

Samsonov A, Yu JZ, Rasenick M, Popov SV. 2004. Tau interaction with microtubules in vivo. Journal of Cell Science. 117:6129-6141.

Scholz T, Mandelkow E. 2014. Transport and diffusion of tau protein in neurons. Cellular and Molecular Life Sciences. 71:3139-3150.

Sleigh JN, Rossor AM, Fellows AD, Tosolini AP, Schiavo G. 2019. Axonal transport and neurological disease. Nature Reviews Neurology. 15:691-703.

Utton M, Connell J, Asuni A, van Slegtenhorst M, Hutton M, de Silva R, Lees A, Miller C, Anderton B. 2002. The slow axonal transport of the microtubule-associated protein tau and the transport rates of different isoforms and mutants in cultured neurons. Journal of Neuroscience. 22:6394-6400.

Utton M, Noble W, Hill J, Anderton B, Hanger D. 2005. Molecular motors implicated in the axonal transport of tau and alpha-synuclein. Journal of Cell Science. 118:4645-4654.

Wang L, Ho CL, Sun DM, Liem RKH, Brown A. 2000. Rapid movement of axonal neurofilaments interrupted by prolonged pauses. Nature Cell Biology. 2:137-141.

Weissmann C, Reyher H, Gauthier A, Steinhoff H, Junge W, Brandt R. 2009. Microtubule binding and trapping at the tip of neurites regulate tau motion in living neurons. Traffic. 10:1655-1668.

Yang X, Huang X. 2004. Lower-order penalty methods for mathematical programs with complementarity constraints. Optimization Methods & Software. 19:693-720.

Zadeh KS. 2008. Parameter estimation in flow through partially saturated porous materials. Journal of Computational Physics. 227:10243-10262.

Zadeh KS. 2011. A synergic simulation-optimization approach for analyzing biomolecular dynamics in living organisms. Computers in Biology and Medicine. 41:24-36.

Zadeh KS, Montas HJ. 2014. Parametrization of flow processes in porous media by multiobjective inverse modeling. Journal of Computational Physics. 259:390-401.

Zadeh KS, Shah SB. 2010. Mathematical modeling and parameter estimation of axonal cargo transport. Journal of Computational Neuroscience. 28:495-507.

Zempell H, Mandelkow E. 2014. Lost after translation: Missorting of tau protein and consequences for Alzheimer disease. Trends in Neurosciences. 37:721-732.

Figure captions

Fig. 1. A diagram of a neuron showing various modes of SAT and diffusion of tau. In displaying possible mechanisms of tau transport, we followed Scholz and Mandelkow (2014) (see Fig. 3 in Scholz and Mandelkow (2014)). Tau can be transported by molecular motors, kinesin and dynein (active transport), or by a diffusion-driven mechanism, either in the cytosol or by diffusion along MTs. Motor-driven retrograde transport of tau may occur by tau piggybacking on short microtubule fragments translocated by cytoplasmic dynein.

Fig. 2. A kinetic diagram displaying seven kinetic states in our model of tau transport in the axon.

Fig. 3. (a) Total concentration of tau. The solution for a full SAT model, which accounts for four mechanisms of tau transport (anterograde and retrograde SAT as well as tau diffusion in the cytosol and along MTs), was obtained numerically. The solution for a model that accounts for anterograde (kinesin-driven) transport only was obtained analytically, since for this case the closed-form solution given by Eqs. (23), (27), and (30)-(34) is available. Experimental data from Fig. 7D of Black et al. (1996) are shown by open circles. These data were rescaled such that the experimentally measured tau concentration at the axon hillock (at $x^* = 0$) was equal to unity. (b) Total flux of tau versus position in the axon, for the full SAT model and the model that simulates anterograde motor-driven transport only.

Fig. 4. (a) Concentration of cytosolic tau that can freely diffuse and can be degraded in proteasomes. (b) Average velocity of tau. The range of the average tau velocity reported in Mercken et al. (1995) is shown by a horizontal band. Distributions for the full SAT model and the model that simulates anterograde motor-driven transport only are displayed.

Fig. 5. (a) Percentage of MT-bound tau versus position in the axon, for the full SAT model and the model that simulates anterograde motor-driven transport only. (b) Total concentration of tau and seven of its components for the model that simulates anterograde motor-driven transport only. The fact that the model with anterograde motor-driven transport only predicts tau distributions that are given by horizontal lines suggests that accounting for other mechanisms of tau transport (in addition to anterograde motor-driven transport) is required to simulate a variation of tau distribution along the axon length.

Figure 1

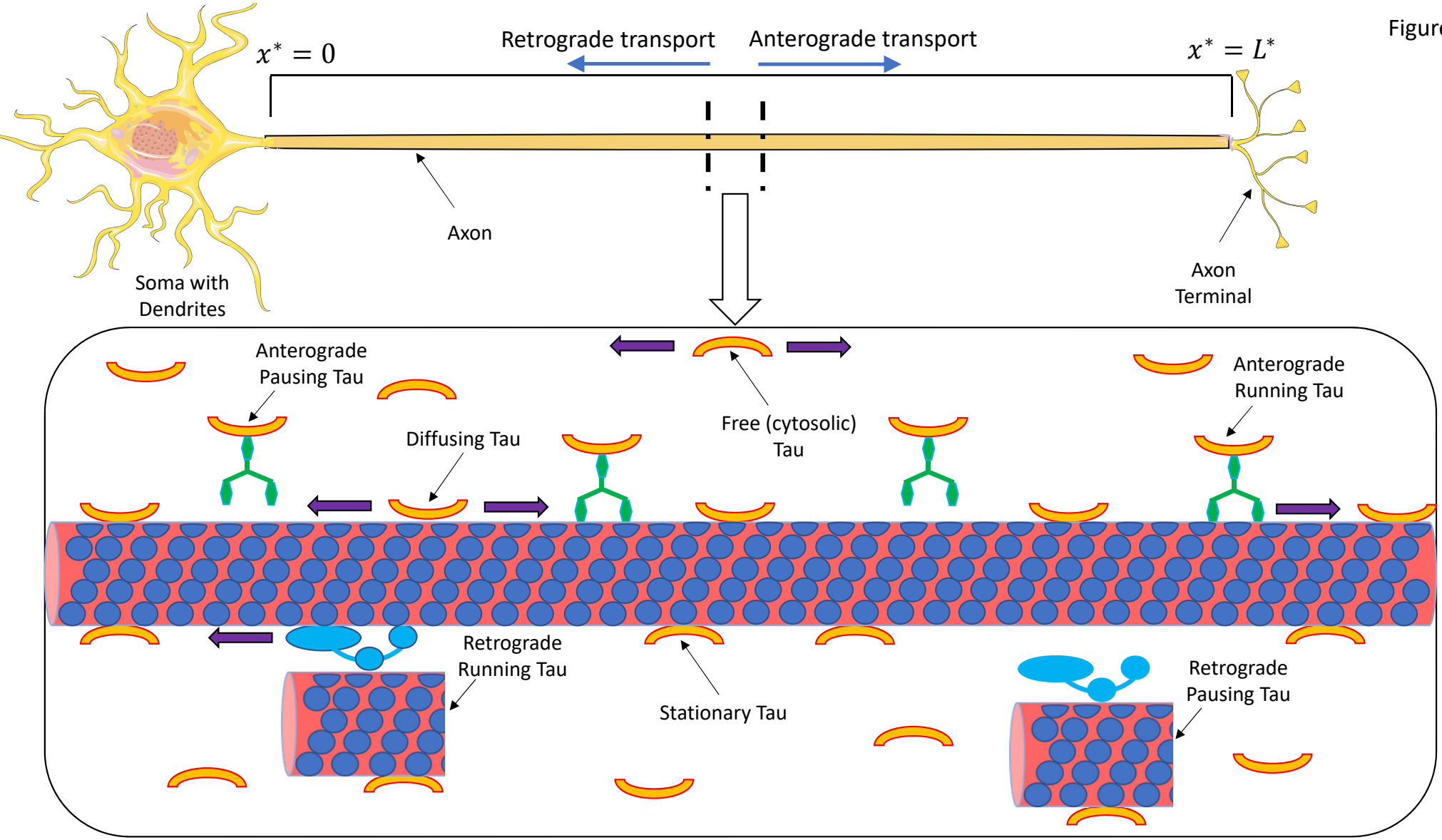
$x^* = 0$
Retrograde transport
Anterograde transport
$x^* = L^*$
Axon
Soma with Dendrites
Axon Terminal
Anterograde Pausing Tau
Free (cytosolic) Tau
Anterograde Running Tau
Diffusing Tau
Retrograde Running Tau
Stationary Tau
Retrograde Pausing Tau

Figure 2

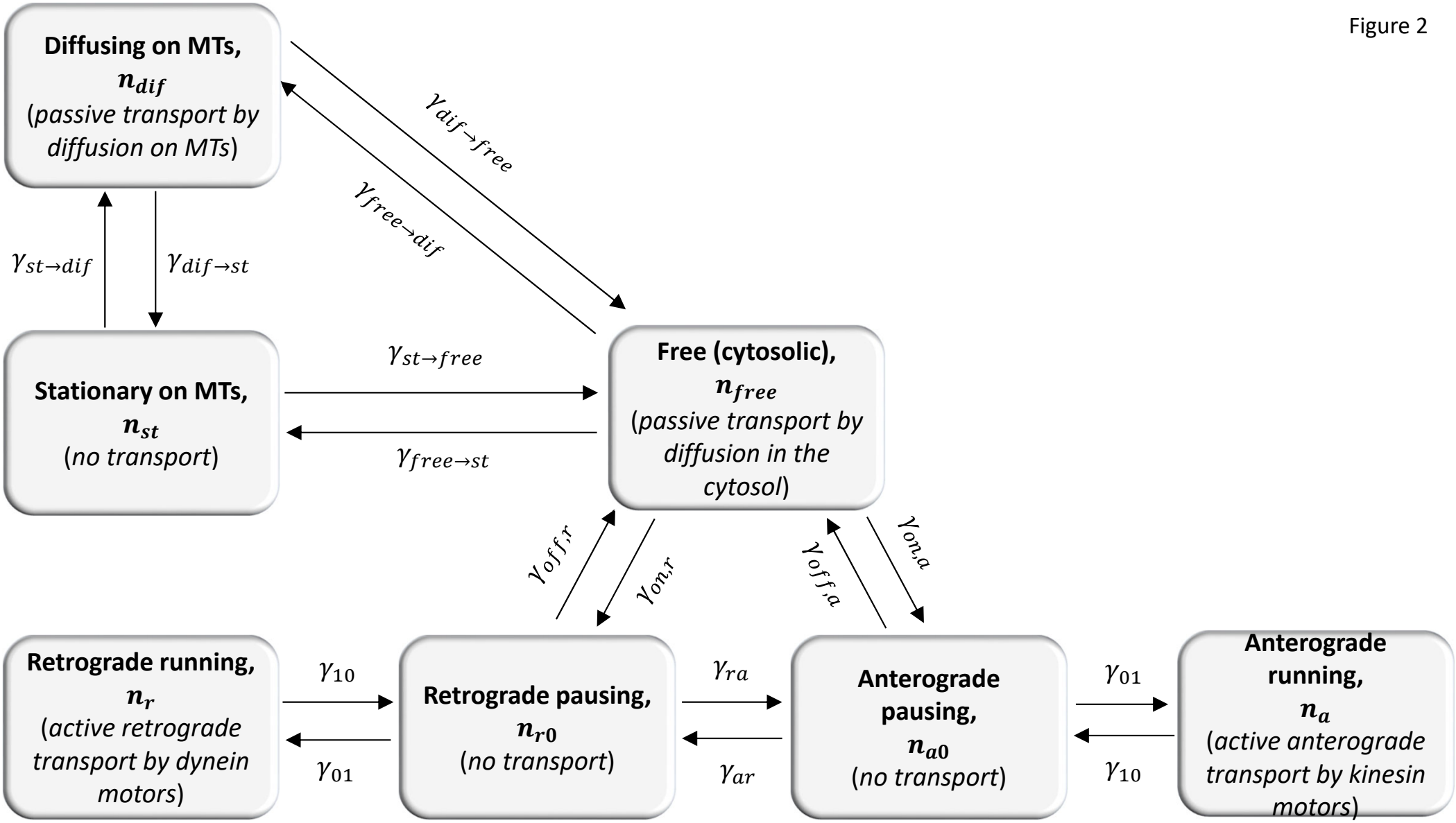
Diffusing on MTs, n_{dif} (passive transport by diffusion on MTs)
$\gamma_{dif\to free}$
$\gamma_{free\to dif}$
$\gamma_{st\to dif}$
$\gamma_{dif\to st}$
Stationary on MTs, n_{st} (no transport)
$\gamma_{st\to free}$
$\gamma_{free\to st}$
Free (cytosolic), n_{free} (passive transport by diffusion in the cytosol)
$\gamma_{off,r}$
$\gamma_{on,r}$
$\gamma_{off,a}$
$\gamma_{on,a}$
Retrograde running, n_r (active retrograde transport by dynein motors)
γ_{10}
γ_{01}
Retrograde pausing, n_{r0} (no transport)
γ_{ra}
γ_{ar}
Anterograde pausing, n_{a0} (no transport)
γ_{01}
γ_{10}
Anterograde running, n_a (active anterograde transport by kinesin motors)

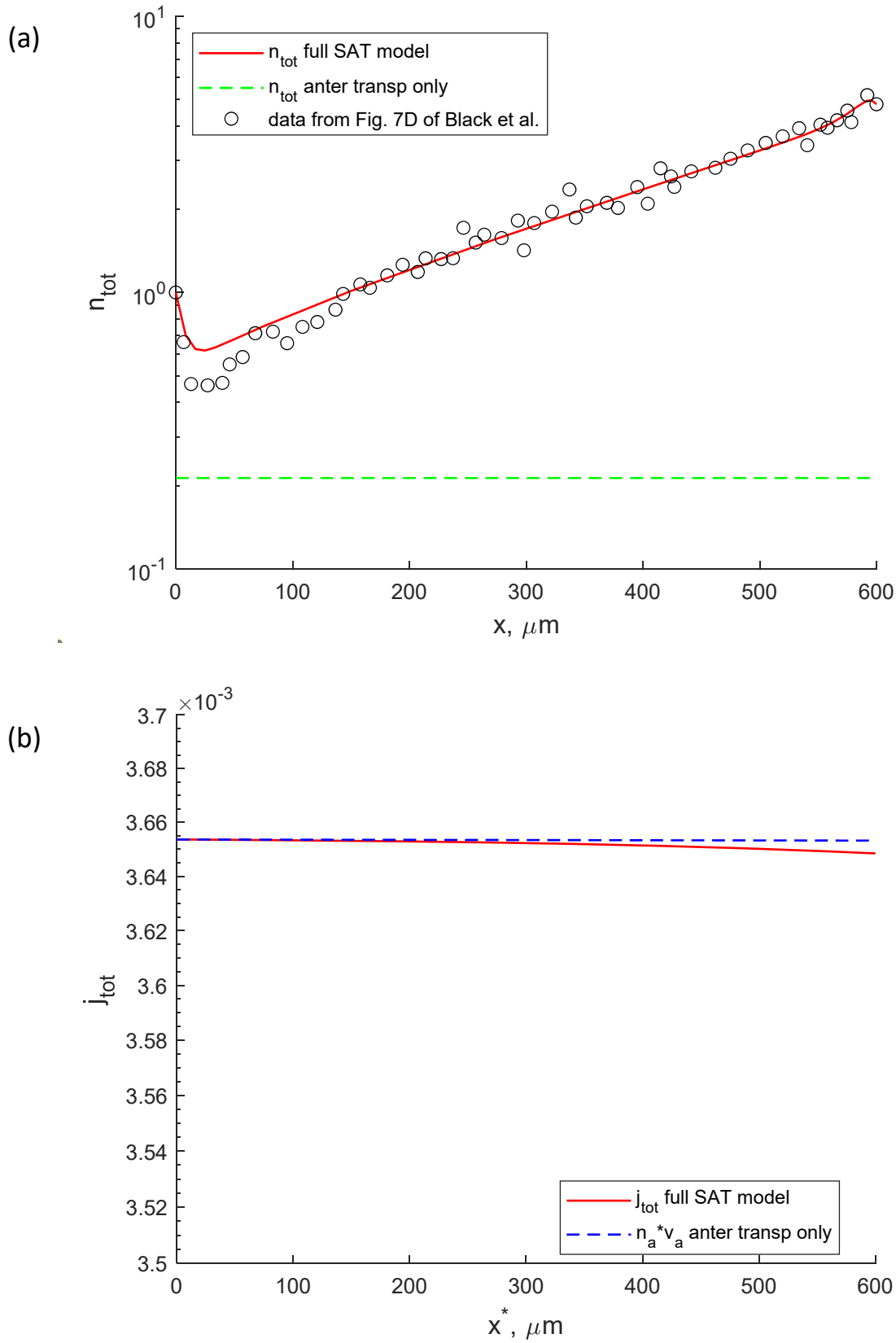
(a)
10^1
10^0
10^{-1}
n_{tot}
n_{tot} full SAT model
n_{tot} anter transp only
data from Fig. 7D of Black et al.
0
100
200
300
400
500
600
x, μm
(b)
$\times 10^{-3}$
3.7
3.68
3.66
3.64
3.62
3.6
3.58
3.56
3.54
3.52
3.5
j_{tot}
j_{tot} full SAT model
n_a*v_a anter transp only
0
100
200
300
400
500
600
x^*, μm

Figure 3

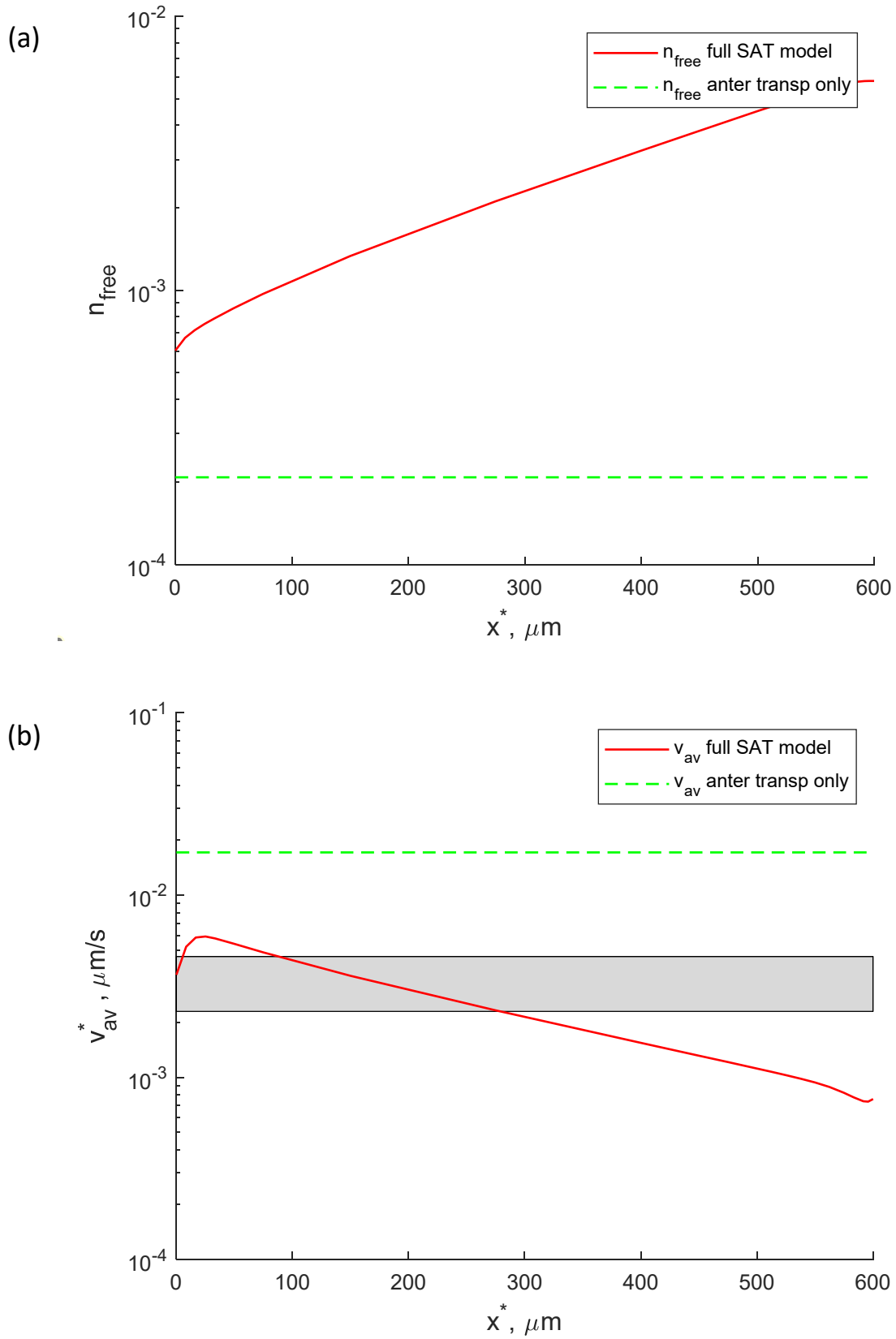
(a)
10^{-2}
10^{-3}
10^{-4}
n_{free}
n_{free} full SAT model
n_{free} anter transp only
0
100
200
300
400
500
600
x^*, μm
(b)
10^{-1}
10^{-2}
10^{-3}
10^{-4}
v^*_{av}, μm/s
v_{av} full SAT model
v_{av} anter transp only
0
100
200
300
400
500
600
x^*, μm

Figure 4

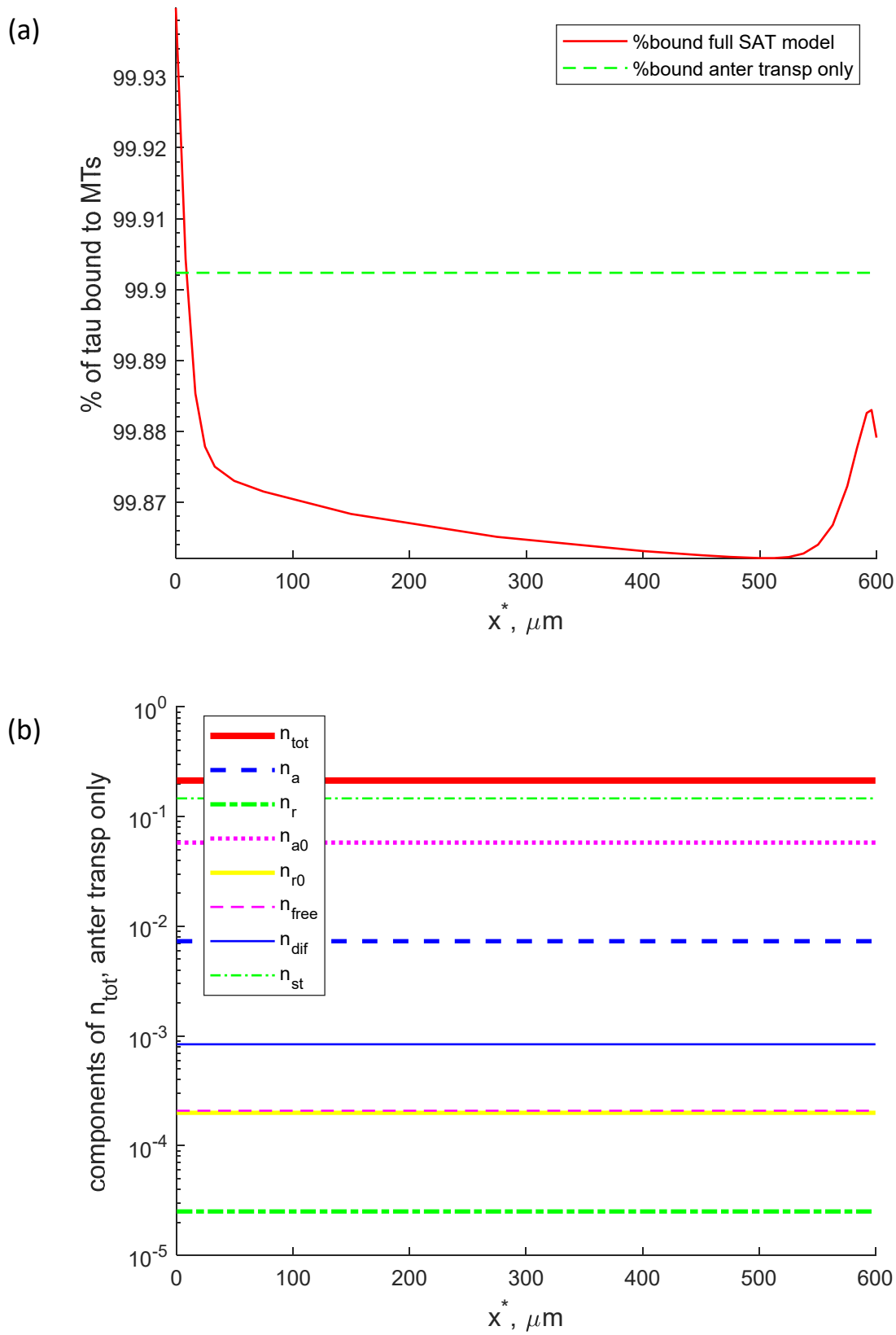
(a)
%bound full SAT model
%bound anter transp only
% of tau bound to MTs
99.93
99.92
99.91
99.9
99.89
99.88
99.87
0
100
200
300
400
500
600
x*, μm
(b)
n_tot
n_a
n_r
n_a0
n_r0
n_free
n_dif
n_st
components of n_tot, anter transp only
10^0
10^-1
10^-2
10^-3
10^-4
10^-5
0
100
200
300
400
500
600
x*, μm

Figure 5

Why slow axonal transport is bidirectional – can axonal transport of tau protein rely only on motor-driven anterograde transport?

Ivan A. Kuznetsov[(a), (b)] and Andrey V. Kuznetsov[(c)]

[(a)]Perelman School of Medicine, University of Pennsylvania, Philadelphia, PA 19104, USA

[(b)]Department of Bioengineering, University of Pennsylvania, Philadelphia, PA 19104, USA

[(c)]Dept. of Mechanical and Aerospace Engineering, North Carolina State University, Raleigh, NC 27695-7910, USA; e-mail: avkuznet@ncsu.edu

Supplemental Materials

S1. Supplementary tables

Table S1. Parameters of the model that were estimated based on values found in literature.

Symbol	Definition	Unit	Estimated value	Reference or estimation method
D^*_{free}	Diffusivity of tau in the cytosolic state	$\mu m^2/s$	11	Scholz and Mandelkow (2014), Konzack et al. (2007)
D^*_{mt}	Diffusivity of tau along MTs	$\mu m^2/s$	0.153[a]	Hinrichs et al. (2012)
L^*	Length of the axon	μm	600	Black et al. (1996)
$T^*_{1/2}$	Half-life of free monomeric tau	s	2.16×10^5	Poppek et al. (2006)
v^*_a, v^*_r	Velocities of rapid motions of tau on MTs propelled by kinesin and dynein motors, respectively	μm/s	0.5, 0.5	Konzack et al. (2007)

[a] Approximately half of MT-bound tau can diffuse bidirectionally along MTs, while the rest remain stationary (Hinrichs et al. 2012).

Table S2. Parameters that characterize transport of tau in the axon and their estimated values. The values reported here are different from those reported in Kuznetsov and Kuznetsov (2017) because we now used a different value of D^*_{free}. LSR (Least Square Regression), Beck and Arnold (1977).

Symbol	Definition	Unit	Estimated value	Reference or estimation method
γ^*_{10}	Kinetic constant describing the rate of transitions $n^*_a \to n^*_{a0}$ and $n^*_r \to n^*_{r0}$	s^{-1}	1.744×10^{-1} [a]	LSR
γ^*_{01}	Kinetic constant describing the rate of transitions $n^*_{a0} \to n^*_a$ and $n^*_{r0} \to n^*_r$	s^{-1}	2.198×10^{-2} [a]	LSR
γ^*_{ar}	Kinetic constant describing the rate of transition $n^*_{a0} \to n^*_{r0}$	s^{-1}	1.890×10^{-5}	LSR
γ^*_{ra}	Kinetic constant describing the rate of transition $n^*_{r0} \to n^*_{a0}$	s^{-1}	5.529×10^{-3}	LSR
$\gamma^*_{on,a}$	Kinetic constant describing the rate of transition $n^*_{free} \to n^*_{a0}$	s^{-1}	6.050×10^{-5}	LSR

$\gamma^*_{on,r}$	Kinetic constant describing the rate of transition $n^*_{free} \rightarrow n^*_{r0}$	s^{-1}	6.816×10^{-5}	LSR
$\gamma^*_{off,a}$	Kinetic constant describing the rate of transition $n^*_{a0} \rightarrow n^*_{free}$	s^{-1}	3.289×10^{-7}	LSR
$\gamma^*_{off,r}$	Kinetic constant describing the rate of transition $n^*_{r0} \rightarrow n^*_{free}$	s^{-1}	4.201×10^{-5}	LSR
$\gamma^*_{free\rightarrow st}$	Kinetic constant describing the rate of transition $n^*_{free} \rightarrow n^*_{st}$	s^{-1}	7.246×10^{-3}	LSR
$\gamma^*_{st\rightarrow free}$	Kinetic constant describing the rate of transition $n^*_{st} \rightarrow n^*_{free}$	s^{-1}	1.817×10^{-5}	LSR
$\gamma^*_{free\rightarrow dif}$	Kinetic constant describing the rate of transition $n^*_{free} \rightarrow n^*_{dif}$	s^{-1}	7.307×10^{-3}	LSR
$\gamma^*_{dif\rightarrow free}$	Kinetic constant describing the rate of transition $n^*_{dif} \rightarrow n^*_{free}$	s^{-1}	4.359×10^{-4}	LSR
$\gamma^*_{dif\rightarrow st}$	Kinetic constant describing the rate of transition $n^*_{dif} \rightarrow n^*_{st}$	s^{-1}	5.281×10^{-3}	LSR
$\gamma^*_{st\rightarrow dif}$	Kinetic constant describing the rate of transition $n^*_{st} \rightarrow n^*_{dif}$	s^{-1}	2.240×10^{-5}	LSR

$j_{tot,x=0}$ [b]	Dimensionless total flux of tau from the soma into the axon		3.654×10^{-3}	LSR
$n_{free,x=0}$ [c]	Dimensionless concentration of free (cytosolic) tau at the axon hillock		6.030×10^{-4}	LSR
A	Coefficient in Eq. (S1)		3.254×10^{-1}	LSR

[a] Values of γ_{10}^{*} and γ_{01}^{*} given in Table S2 are effective values of these kinetic constants, which give the best fit of model predictions with experimental or interpolated data. The dwell time of tau on MTs may be as short as 40 ms (Janning et al. 2014; Igaev et al. 2014).

[b] $j_{tot,x=0} = \dfrac{j_{tot,x=0}^{*}}{n_{tot,x=0}^{*} v_{a}^{*}}$.

[c] $n_{free,x=0} = \dfrac{n_{free,x=0}^{*}}{n_{tot,x=0}^{*}}$.

Table S3. Dimensionless dependent variables in the model of tau transport.

Symbol	Definition
j_{tot}	$\dfrac{j_{tot}^{*}}{n_{tot,x=0}^{*} v_{a}^{*}}$
n_{tot}	$\dfrac{n_{tot}^{*}}{n_{tot,x=0}^{*}}$
n_{a}	$\dfrac{n_{a}^{*}}{n_{tot,x=0}^{*}}$

n_r	$\frac{n_r^*}{n_{tot,x=0}^*}$
n_{a0}	$\frac{n_{a0}^*}{n_{tot,x=0}^*}$
n_{r0}	$\frac{n_{r0}^*}{n_{tot,x=0}^*}$
n_{free}	$\frac{n_{free}^*}{n_{tot,x=0}^*}$
n_{st}	$\frac{n_{st}^*}{n_{tot,x=0}^*}$
n_{dif}	$\frac{n_{dif}^*}{n_{tot,x=0}^*}$

S2. Estimating the flux of tau into the axon terminal

To estimate the flux of tau into the axon terminal, $j_{tot,x=L}^*$, we used the approach developed in Li et al. (2012) for modeling the transport of neurofilament proteins. Tau that enters the axon terminal can either be degraded or reverse its direction of motion to retrograde and re-enter the axon. If γ_{deg}^* is a kinetic constant characterizing tau degradation rate and t_{rev}^* is the time required for a motor-driven tau to reverse its direction in the terminal, then the probability of tau degradation is estimated as $1-\exp\left[-\gamma_{deg}^* t_{rev}^*\right]$. γ_{deg}^* is estimated as $\ln(2)/T_{1/2}^*$ and t_{rev}^* is estimated as $1/\gamma_{ar}^*$. Since this estimate is approximate, we multiplied this estimate by a parameter *A*, as we did in Kuznetsov and Kuznetsov (2017). The value of parameter *A* is determined by finding the best fit with published experimental data. This leads to the following equation:

$$j_{tot,x=L}^* = A\left(1-\exp\left[-\frac{\ln(2)}{T_{1/2}^*}\frac{1}{\gamma_{ar}^*}\right]\right)v_a^* n_a^* . \qquad \text{(S1)}$$

S3. Numerical solution of equations simulating SAT of tau and finding the best-fit parameter values

Eqs. (1)-(7) compose a system that contains ordinary differential equations and algebraic equations. We used algebraic Eqs. (3), (4), and (7) to eliminate n_{a0}^*, n_{r0}^*, and n_{st}^* from the remaining equations. The remaining equations were solved subject to boundary conditions (12), (13) using the MATLAB's BVP4C solver (MATLAB R2019a, MathWorks, Natick, MA, USA), Kuznetsov and Kuznetsov (2018).

The penalty function given by Eq. (14) was minimized using MULTISTART with the local solver FMINCON, which are part of MATLAB's Optimization Toolbox. We used the default interior-point algorithm option in FMINCON, which is described in Dantzig and Thapa (2003). 10,000 randomly selected starting points were used in MULTISTART.

S4. Simplified equations

S4.1. Simplified equations for $v_r^* \to 0$

$$-v_a^* \frac{dn_a^{*(0)}}{dx^*} - \gamma_{10}^* n_a^{*(0)} + \gamma_{01}^* n_{a0}^{*(0)} = 0\,, \tag{S2}$$

$$-\gamma_{10}^* n_r^{*(0)} + \gamma_{01}^* n_{r0}^{*(0)} = 0\,, \tag{S3}$$

$$-\left(\gamma_{01}^* + \gamma_{ar}^* + \gamma_{off,a}^*\right) n_{a0}^{*(0)} + \gamma_{10}^* n_a^{*(0)} + \gamma_{ra}^* n_{r0}^{*(0)} + \gamma_{on,a}^* n_{free}^{*(0)} = 0\,, \tag{S4}$$

$$-\left(\gamma_{01}^* + \gamma_{ra}^* + \gamma_{off,r}^*\right) n_{r0}^{*(0)} + \gamma_{10}^* n_r^{*(0)} + \gamma_{ar}^* n_{a0}^{*(0)} + \gamma_{on,r}^* n_{free}^{*(0)} = 0\,, \tag{S5}$$

$$D_{free}^* \frac{d^2 n_{free}^{*(0)}}{dx^{*2}} + \gamma_{off,a}^* n_{a0}^{*(0)} + \gamma_{off,r}^* n_{r0}^{*(0)} - \left(\gamma_{on,a}^* + \gamma_{on,r}^* + \gamma_{free\to st}^* + \gamma_{free\to dif}^*\right) n_{free}^{*(0)} + \gamma_{st\to free}^* n_{st}^{*(0)}$$

$$+\gamma_{dif\to free}^* n_{dif}^{*(0)} - \frac{n_{free}^{*(0)} \ln(2)}{T_{1/2}^*} = 0\,, \tag{S6}$$

$$D_{mt}^* \frac{d^2 n_{dif}^{*(0)}}{dx^{*2}} - \left(\gamma_{dif\to free}^* + \gamma_{dif\to st}^*\right) n_{dif}^{*(0)} + \gamma_{free\to dif}^* n_{free}^{*(0)} + \gamma_{st\to dif}^* n_{st}^{*(0)} = 0\,, \tag{S7}$$

$$-\left(\gamma_{st\to free}^* + \gamma_{st\to dif}^*\right) n_{st}^{*(0)} + \gamma_{free\to st}^* n_{free}^{*(0)} + \gamma_{dif\to st}^* n_{dif}^{*(0)} = 0\,. \tag{S8}$$

S4.2. Simplified equations for $v_r^* \to 0$ and $D_{free}^* \to 0$

$$-v_a^* \frac{dn_a^{*(0,0)}}{dx^*} - \gamma_{10}^* n_a^{*(0,0)} + \gamma_{01}^* n_{a0}^{*(0,0)} = 0 , \tag{S9}$$

$$-\gamma_{10}^* n_r^{*(0,0)} + \gamma_{01}^* n_{r0}^{*(0,0)} = 0 , \tag{S10}$$

$$-\left(\gamma_{01}^* + \gamma_{ar}^* + \gamma_{off,a}^*\right) n_{a0}^{*(0,0)} + \gamma_{10}^* n_a^{*(0,0)} + \gamma_{ra}^* n_{r0}^{*(0,0)} + \gamma_{on,a}^* n_{free}^{*(0,0)} = 0 , \tag{S11}$$

$$-\left(\gamma_{01}^* + \gamma_{ra}^* + \gamma_{off,r}^*\right) n_{r0}^{*(0,0)} + \gamma_{10}^* n_r^{*(0,0)} + \gamma_{ar}^* n_{a0}^{*(0,0)} + \gamma_{on,r}^* n_{free}^{*(0,0)} = 0 , \tag{S12}$$

$$\gamma_{off,a}^* n_{a0}^{*(0,0)} + \gamma_{off,r}^* n_{r0}^{*(0,0)} - \left(\gamma_{on,a}^* + \gamma_{on,r}^* + \gamma_{free\to st}^* + \gamma_{free\to dif}^*\right) n_{free}^{*(0,0)} + \gamma_{st\to free}^* n_{st}^{*(0,0)}$$

$$+\gamma_{dif\to free}^* n_{dif}^{*(0,0)} - \frac{n_{free}^{*(0,0)} \ln(2)}{T_{1/2}^*} = 0 , \tag{S13}$$

$$D_{mt}^* \frac{d^2 n_{dif}^{*(0,0)}}{dx^{*2}} - \left(\gamma_{dif\to free}^* + \gamma_{dif\to st}^*\right) n_{dif}^{*(0,0)} + \gamma_{free\to dif}^* n_{free}^{*(0,0)} + \gamma_{st\to dif}^* n_{st}^{*(0,0)} = 0 , \tag{S14}$$

$$-\left(\gamma_{st\to free}^* + \gamma_{st\to dif}^*\right) n_{st}^{*(0,0)} + \gamma_{free\to st}^* n_{free}^{*(0,0)} + \gamma_{dif\to st}^* n_{dif}^{*(0,0)} = 0 . \tag{S15}$$

S4.3. Simplified equations for $v_r^* \to 0$, $D_{free}^* \to 0$, and $D_{mt}^* \to 0$

$$-v_a^* \frac{dn_a^{*(0,0,0)}}{dx^*} - \gamma_{10}^* n_a^{*(0,0,0)} + \gamma_{01}^* n_{a0}^{*(0,0,0)} = 0 , \tag{S16}$$

$$-\gamma_{10}^* n_r^{*(0,0,0)} + \gamma_{01}^* n_{r0}^{*(0,0,0)} = 0 , \tag{S17}$$

$$-\left(\gamma_{01}^* + \gamma_{ar}^* + \gamma_{off,a}^*\right) n_{a0}^{*(0,0,0)} + \gamma_{10}^* n_a^{*(0,0,0)} + \gamma_{ra}^* n_{r0}^{*(0,0,0)} + \gamma_{on,a}^* n_{free}^{*(0,0,0)} = 0 , \tag{S18}$$

$$-\left(\gamma_{01}^* + \gamma_{ra}^* + \gamma_{off,r}^*\right) n_{r0}^{*(0,0,0)} + \gamma_{10}^* n_r^{*(0,0,0)} + \gamma_{ar}^* n_{a0}^{*(0,0,0)} + \gamma_{on,r}^* n_{free}^{*(0,0,0)} = 0 , \tag{S19}$$

$$\gamma_{off,a}^* n_{a0}^{*(0,0,0)} + \gamma_{off,r}^* n_{r0}^{*(0,0,0)} - \left(\gamma_{on,a}^* + \gamma_{on,r}^* + \gamma_{free\to st}^* + \gamma_{free\to dif}^*\right) n_{free}^{*(0,0,0)} + \gamma_{st\to free}^* n_{st}^{*(0,0,0)}$$

$$+\gamma_{dif\to free}^* n_{dif}^{*(0,0,0)} - \frac{n_{free}^{*(0,0,0)} \ln(2)}{T_{1/2}^*} = 0 , \tag{S20}$$

$$-\left(\gamma_{dif\to free}^* + \gamma_{dif\to st}^*\right) n_{dif}^{*(0,0,0)} + \gamma_{free\to dif}^* n_{free}^{*(0,0,0)} + \gamma_{st\to dif}^* n_{st}^{*(0,0,0)} = 0 , \tag{S21}$$

$$-\left(\gamma_{st\to free}^* + \gamma_{st\to dif}^*\right) n_{st}^{*(0,0,0)} + \gamma_{free\to st}^* n_{free}^{*(0,0,0)} + \gamma_{dif\to st}^* n_{dif}^{*(0,0,0)} = 0 . \tag{S22}$$

S4.4. Simplified equations after $n_{r0}^{*[0]}$ was eliminated using Eq. (S17)

$$-v_a^* \frac{dn_a^{*[0]}}{dx^*} - \gamma_{10}^* n_a^{*[0]} + \gamma_{01}^* n_{a0}^{*[0]} = 0\,, \tag{S23}$$

$$-\left(\gamma_{01}^* + \gamma_{ar}^* + \gamma_{off,a}^*\right) n_{a0}^{*[0]} + \gamma_{10}^* n_a^{*[0]} + \gamma_{ra}^* \frac{\gamma_{10}^*}{\gamma_{01}^*} n_r^{*[0]} + \gamma_{on,a}^* n_{free}^{*[0]} = 0\,, \tag{S24}$$

$$-\left(\gamma_{01}^* + \gamma_{ra}^* + \gamma_{off,r}^*\right) \frac{\gamma_{10}^*}{\gamma_{01}^*} n_r^{*[0]} + \gamma_{10}^* n_r^{*[0]} + \gamma_{ar}^* n_{a0}^{*[0]} + \gamma_{on,r}^* n_{free}^{*[0]} = 0\,, \tag{S25}$$

$$\gamma_{off,a}^* n_{a0}^{*[0]} + \gamma_{off,r}^* \frac{\gamma_{10}^*}{\gamma_{01}^*} n_r^{*[0]} - \left(\gamma_{on,a}^* + \gamma_{on,r}^* + \gamma_{free\to st}^* + \gamma_{free\to dif}^*\right) n_{free}^{*[0]} + \gamma_{st\to free}^* n_{st}^{*[0]}$$

$$+\gamma_{dif\to free}^* n_{dif}^{*[0]} - \frac{n_{free}^{*[0]} \ln(2)}{T_{1/2}^*} = 0\,, \tag{S26}$$

$$-\left(\gamma_{dif\to free}^* + \gamma_{dif\to st}^*\right) n_{dif}^{*[0]} + \gamma_{free\to dif}^* n_{free}^{*[0]} + \gamma_{st\to dif}^* n_{st}^{*[0]} = 0\,, \tag{S27}$$

$$-\left(\gamma_{st\to free}^* + \gamma_{st\to dif}^*\right) n_{st}^{*[0]} + \gamma_{free\to st}^* n_{free}^{*[0]} + \gamma_{dif\to st}^* n_{dif}^{*[0]} = 0\,. \tag{S28}$$

S5. Supplementary figures

(a)

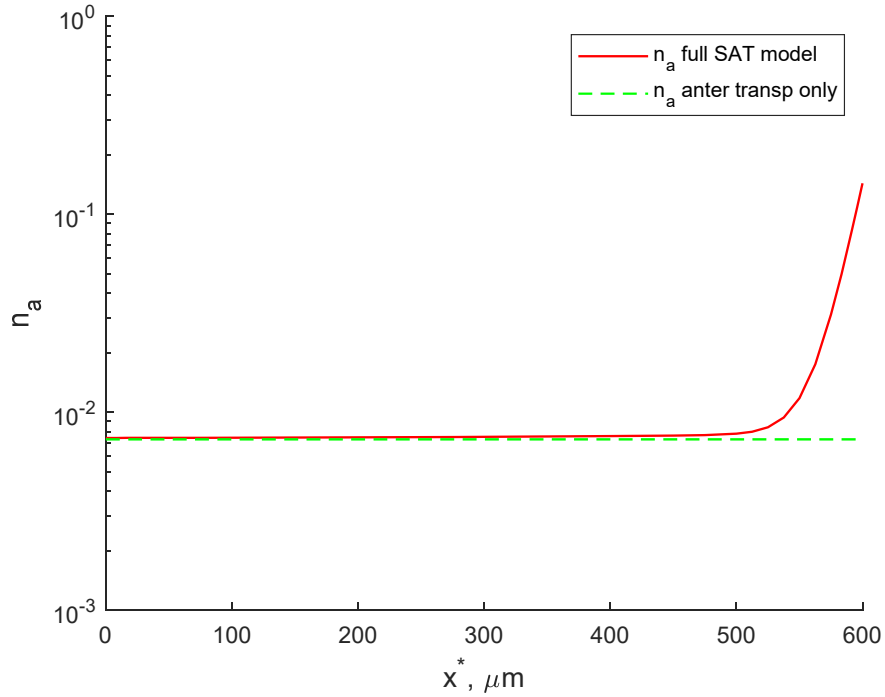
10^0
10^{-1}
10^{-2}
10^{-3}
n_a
0
100
200
300
400
500
600
x^*, μm
n_a full SAT model
n_a anter transp only

(b)

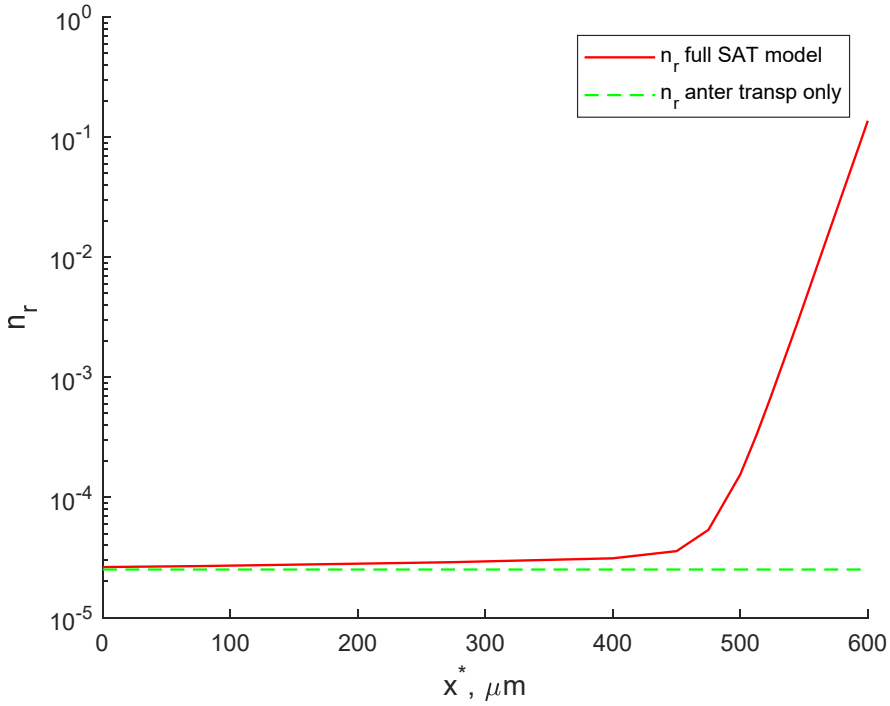
10^0
10^{-1}
10^{-2}
10^{-3}
10^{-4}
10^{-5}
n_r
0
100
200
300
400
500
600
x^*, μm
n_r full SAT model
n_r anter transp only

Fig. S1. (a) Concentration of anterograde kinesin-driven tau. (b) Concentration of retrograde dynein-driven tau. Distributions for the full SAT model and the model that simulates anterograde motor-driven transport only are displayed.

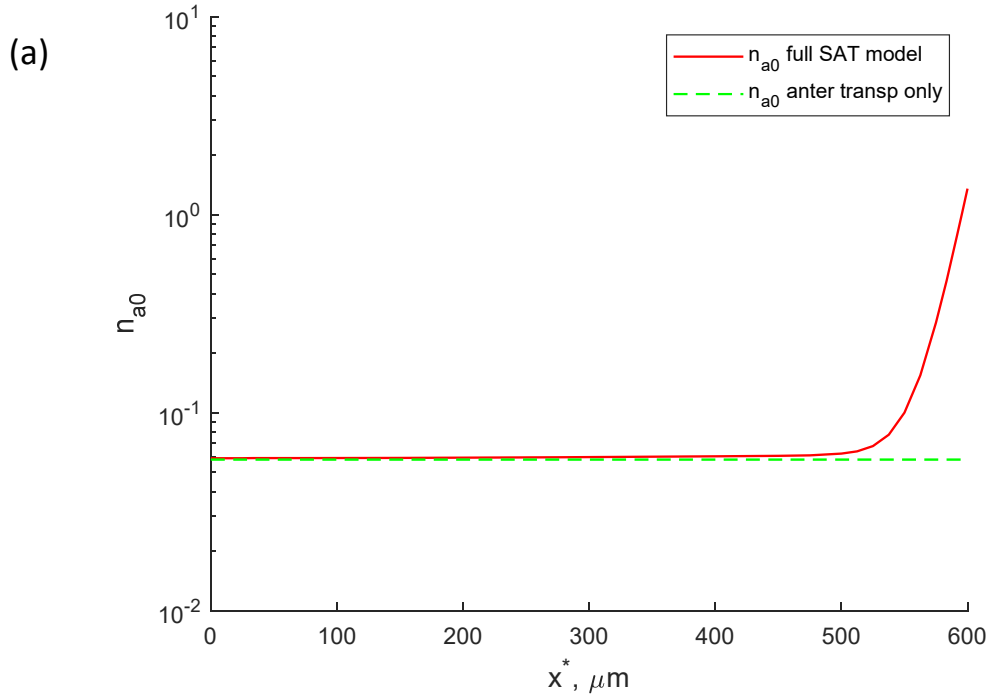

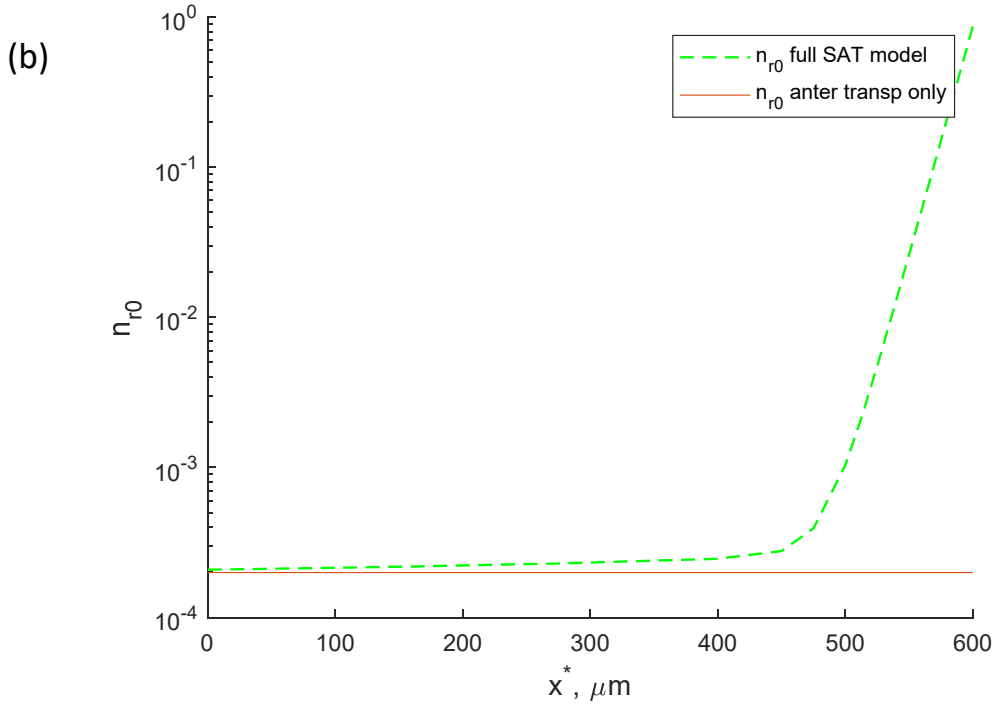

Fig. S2. (a) Concentration of anterograde pausing tau. (b) Concentration of retrograde pausing tau. Distributions for the full SAT model and the model that simulates anterograde motor-driven transport only are displayed.

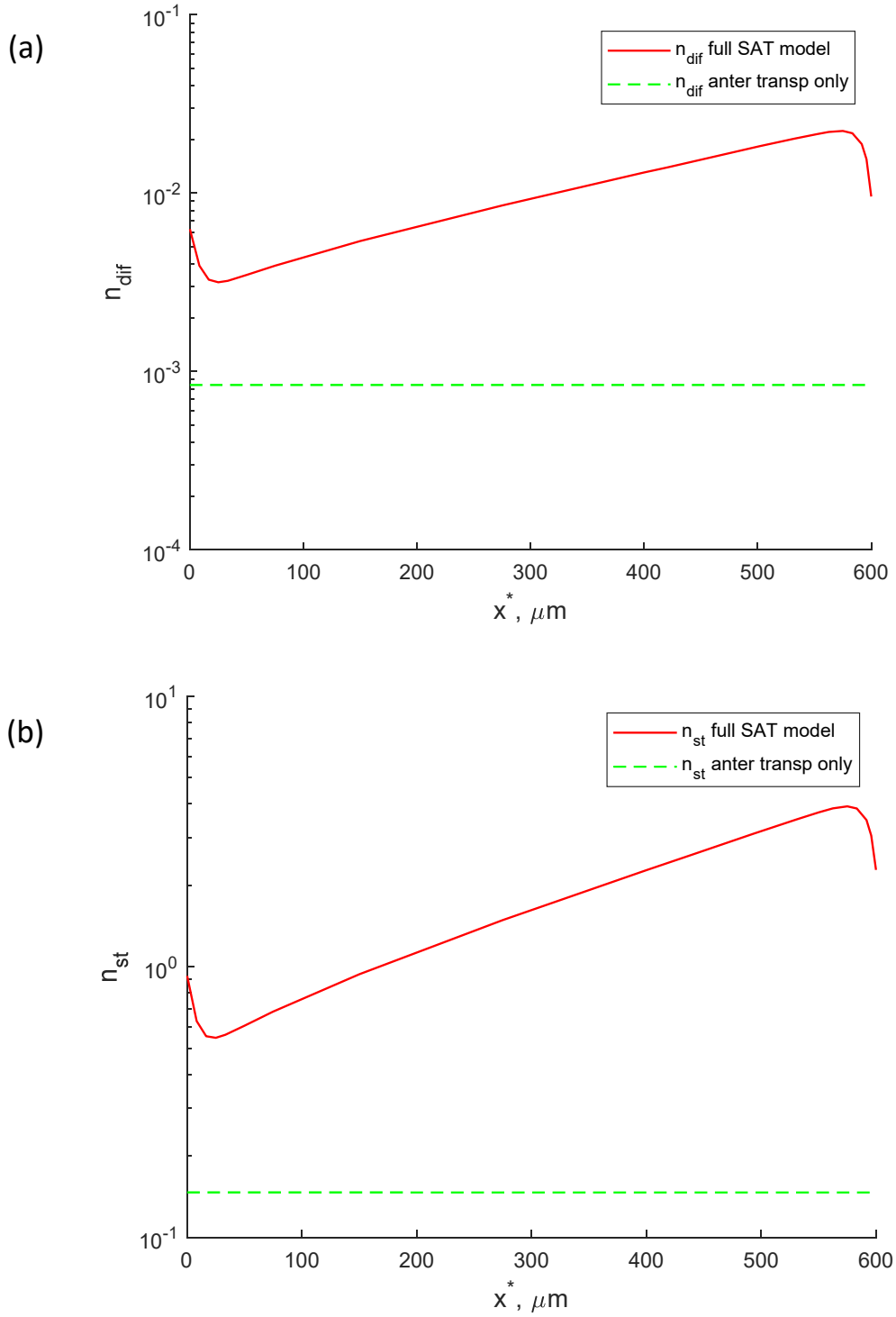

Fig. S3. (a) Concentration of MT-bound tau that can diffuse along MTs. (a) Concentration of MT-bound tau that is stationary on MTs.